Joint Inversion for Surface Accumulation and Geothermal Flux from Ice-Penetrating Radar Observations at Dome A, East Antarctica. Part II: Ice Sheet State and Geophysical Analysis

M.J. Wolovick[1], J.C. Moore[1,2], L. Zhao[1]

[1]College of Global Change and Earth Systems Science, Beijing Normal University, Beijing, China
[2]Arctic Centre, University of Lapland, Rovaniemi, Finland

Key Points:

- Our model matches the observed water and freeze-on locations, predicts new areas to look for water, and estimates freeze-on volume.
- Our model predicts that ice up to 1.5 Ma suitable for coring may be found under the divide, assuming divide stability in the geologic past.
- Our geothermal flux estimate is higher than most previous estimates, reflecting the variability in geothermal flux, even in old cratons.

Corresponding author: Michael Wolovick, `michael.wolovick@gmail.com`

Abstract

Dome A is the peak of the East Antarctic Ice Sheet (EAIS), underlain by the rugged Gamburtsev Subglacial Mountains (GSM). The rugged basal topography produces a complex hydrological system featuring basal melt, water transport and storage, and freeze-on. In a companion paper, we used an inverse model to infer the spatial distributions of geothermal flux and accumulation rate that best fit a vareity of observational constraints. Here, we present and analyze the best-fit state of the ice sheet in detail. Our model agrees well with the observed water bodies and freeze-on structures, while also predicting a significant amount of unobserved water and suggesting a change in stratigraphic interpretation that reduces the volume of the freeze-on units. We predict that a weak Raymond effect underneath the ice divide has been mostly masked by the high-amplitude variability in the layers produced by draping over subglacial topography. Our model stratigraphy agrees well with observations, and we predict- assuming that the ice divide has been stable over time- that there will be two distinct patches of ice older than 1 Ma suitable for ice coring underneath the divide. Finally, our geothermal flux estimate is substantially higher than previous estimates for this region. Correcting for the bias induced by unresolved narrow valleys still leaves our result in the high end of past estimates, with substantial local anomalies that are hotter still. Fundamentally, the observational evidence of a complex basal hydrological system is inconsistent with a simple picture of a uniformly cold East Antarctic craton.

Plain Language Summary

In a companion paper, we combined a model with observations to figure out the best-fit maps of geothermal heat flow and snowfall rate in the highest and coldest part of Antarctica, Dome A. In this paper, we analyze the best-fit model in detail. The observations show liquid water moving around underneath the ice sheet and traveling from melting regions to freezing regions. Our model does a good job of matching those observations, while also suggesting new locations where water underneath the ice may be found and also suggesting that the refrozen ice may be smaller than previously believed. Our model predicts that ice more than one million years old, which would be very useful for collecting ice cores, might be found intact and in order within a narrow region underneath the ice ridge. However, if the ice ridge has moved over time then our model might be wrong about this. Our best-fit map of geothermal heat flow is hotter than previous estimates, even after we try to correct it to account for a possible source of error. This result emphasizes the fact that even old cold areas of Earth's crust can have local areas that are hotter.

1 Introduction

Dome A is the highest and coldest part of the East Antarctic Ice Sheet (EAIS), with a maximum surface elevation of nearly 4100 m and an annual average surface temperature of roughly -60 °C (Fretwell et al., 2013; Comiso, 2000). It is underlain by the Gamburtsev Subglacial Mountains (GSM), a rugged mountain range with $\sim$ 2500 m of relief that is completely covered by the ice sheet (Fig 1). The GSM is believed to have formed by rejuvenation of a Proterozoic crustal root during Permian and Cretaceous rifting (Ferraccioli et al., 2011). Despite the fact that the GSM have been covered by the EAIS continuously since 34 ma, their topography is still dominated by a pre-glacial fluvial valley network modified slightly by valley glaciers in the very early stages of Antarctic glaciation (Bo et al., 2009; Rose et al., 2013). The modern ice divide is located roughly over the northern spur of the GSM, while the southern spur of the mountains is associated with a number of locations where the hydraulic potential would force subglacial water, if present, to flow uphill towards the thinner ice located over the mountain peaks (Fig 1).

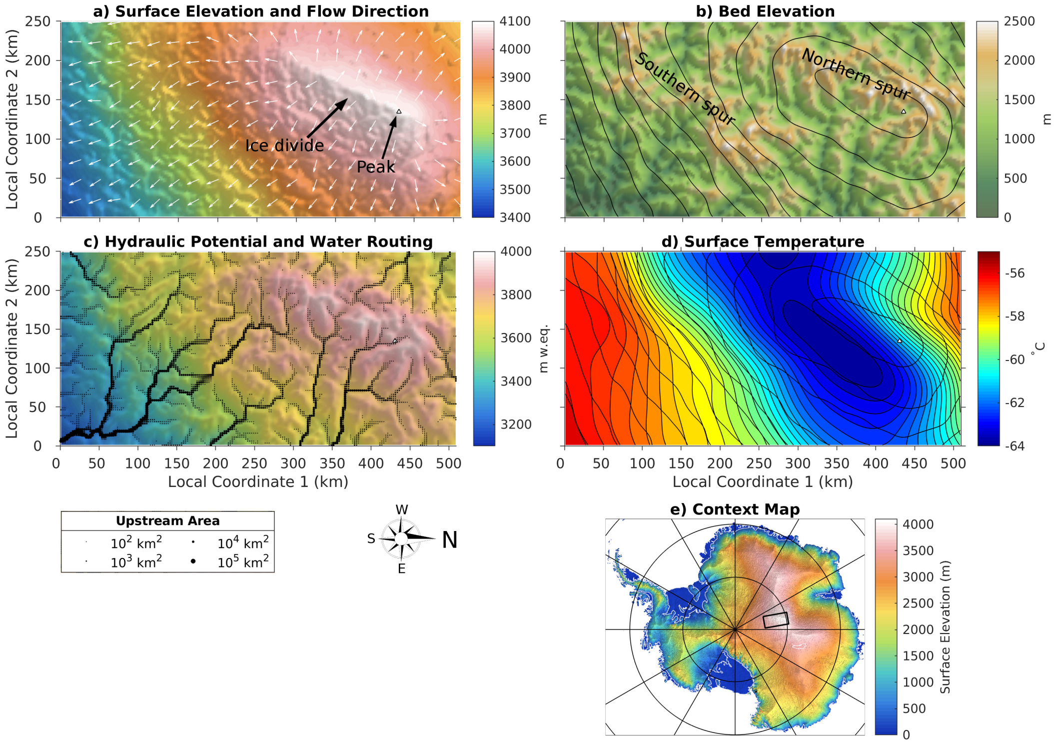

Figure 1. Glaciological setting and boundary conditions for the model. a) Hillshaded ice sheet surface elevation, with flow direction vectors from the smoothed surface overlain; b) hillshaded bed elevation, with 50 m surface contours overlain; c) hillshaded hydraulic potential, with the results of a water routing algorithm overlain; d) surface temperature, with 50 m contours of surface elevation; and e) context map showing model domain (black rectangle) overlain on a plot of hillshaded surface elevation for all of Antarctica. Triangles show Kunlun station near the peak of Dome A. All hillshading performed using two perpendicular light sources at the top and right of the page. Compass rose shows orientation of model domain relative to true north. All subsequent map figures retain this orientation, as well as the local coordinate system aligned with the rectangular domain. Text labels in (a) and (b) indicate geographic features referred to later in the text. Surface and bed elevations are from BEDMAP2 (Fretwell et al., 2013); hydraulic potential has been computed from those quantities using densities of $\rho_i = 917$ and $\rho_w = 1000$ kgm^{-3}, followed by filling of closed basins; and surface temperature is derived from (Comiso, 2000) via the ALBMAP_v1 compilation (Le Brocq et al., 2010), followed by a uniform downward adjustment of 5.75 °C to correct for the difference between modern temperatures and long-term average temperatures, with the correction derived based on the EPICA Dome C ice core (Jouzel et al., 2007).

During the 2008-2009 austral summer field season, the Antarctica's GAmburtsev Province (AGAP) expedition surveyed Dome A and the GSM with a suite of airborne geophysics instruments at a flight line spacing of 5 km with 33 km perpendicular tie lines. In addition to revealing the basic contours of the mountainous subglacial topography (Fig 1b), the ice-penetrating radar data collected during this survey also revealed large plumes of refrozen (accreted) ice being added to the ice sheet base and carried downstream in the ice flow (Bell et al., 2011). The source regions for the most prominent of these freeze-on plumes are associated with the termini of organized networks of small subglacial water bodies in places where the hydraulic potential forces water to flow uphill (Wolovick et al., 2013). This freeze-on process is believed to protect the mountain peaks from erosion by the subglacial water that is found in the deep valleys, thus preserving the GSM against erosion (Creyts et al., 2014). However, much about the ice sheet state in the GSM remains unknown, including critical boundary conditions like the geothermal flux and the long-term accumulation rate, as well as the aspects of the ice sheet state that depend on those boundary conditions, such as the thermal structure of the ice sheet and bed, the basal melt rate and water flux, the ice flow and deformation fields, and the age-depth scale.

In a companion paper (Wolovick et al., in review) we used a formal inverse model to assimilate the AGAP radar observations of subglacial water, freeze-on, and internal layers, in order to solve for best-fit geothermal flux and long-term average accumulation rate fields for Dome A. We also used the continental-scale geothermal flux estimate from Martos et al. (2017), which is based on the AGAP aeromagnetic observations for the part of their model within our domain, as an additional constraint. Our forward model computed a self-consistent coupled steady state between the ice sheet flow field, thermal structure, and basal hydrological system. Our basal hydrology model included both both melt and freeze-on, allowing us to track water transport from source to sink while conserving mass and energy at the bed. We also computed the age structure of the ice sheet and the thickness of freeze-on ice. Our inverse model minimized a compound misfit function accounting for all of the available constraints using an evolutionary algorithm followed by local optimization. Readers interested in exploring the details of the forward model, data constraints, and inverse model are encouraged to read the companion paper. We show the best-fit results of the inversion and their uncertainty fields in Figure 2.

Here, we examine the best-fit state of the ice sheet in detail. We explore the thermal structure of the ice sheet and bed, and show how our model correctly captures the placement of the prominent observed water networks and freeze-on plumes, while also predicting the existence of large wet-based areas in the main trunk valleys of the GSM for which the radar evidence of water is weak or ambiguous. Our model also suggests several reasonable changes in interpretation relative to our earlier published works. We also explore the flow, deformation, and age structure of the ice sheet in detail, showing how our model predicts that a weak version of the Raymond effect (Raymond, 1983) ought to be present underneath the ice divide. This weak Raymond effect creates conditions in which extremely old ice- up to $\sim$1.5 Ma- may be found in stratigraphic order for ice coring. We discuss the implications of our best-fit accumulation rate pattern for divide stability and ice coring. We then discuss how our model may be limited by the need to use gridded topography, which necessarily removes short-wavelength variability from the bed, and we estimate the bias introduced by this limitation in our best-fit estimate of geothermal flux. Finally, we compare our best-fit and bias-corrected geothermal flux estimates with other estimates of geothermal flux in the region, and we discuss the implications of those differences for East Antarctic geology.

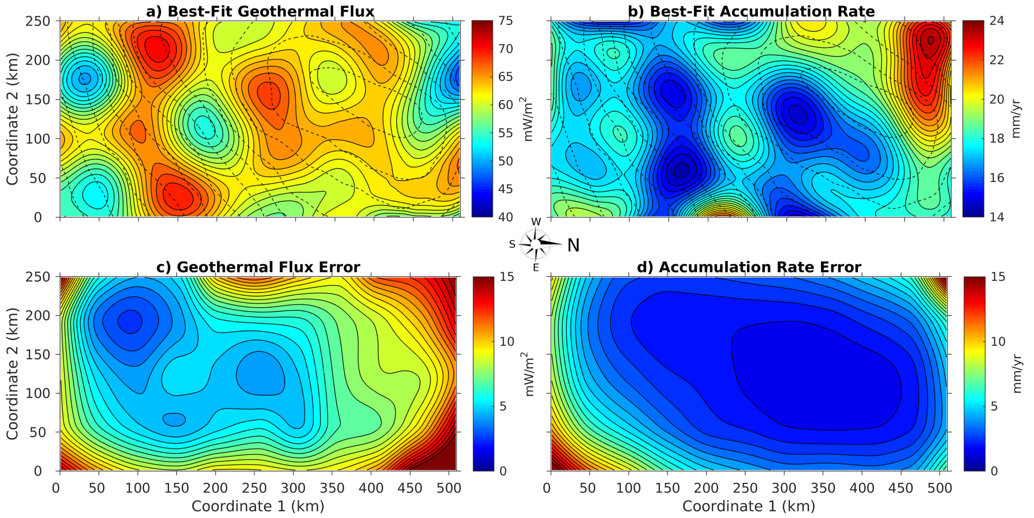

Figure 2. Summary of the results of the inversion described in the companion paper (Wolovick et al., in review). Top row shows best-fit fields for a) geothermal flux and b) accumulation rate, while bottom row (c and d) shows their respective error estimates. Dashed lines in top row are 50m surface elevation contours.

2 Results

2.1 Thermal Structure, Basal Hydrology, and Associated Data Types

The thermal structure of the ice sheet is dominated by conduction, with nearly linear profiles from the bed to the surface (Fig 3a). Because the accumulation rate is so low (Fig 2b), the thermal profiles are only slightly curved by downward advection. Horizontal variability in the thermal state of the ice sheet is strongly influenced by the preglacial valley network of the GSM, with deviations from the simple valley structure where water is forced up and over subglacial ridges (Fig 3, c.f. Fig 1c). To first order, the basal temperature of the ice sheet is determined by basal topography, with ice at the melting point in deep valleys and as much as 25°C below the melting point on the peaks (Fig 3b, c.f. Fig 1b). While basal temperature cannot rise above the melting point, this pattern is continued in the basal melt rate, with the highest melt rates found in the deepest parts of the valleys (Fig 3c). However, the uphill flow of water under the influence of ice overburden pressure feeds freeze-on units and produces important deviations from the simple topographic picture. At five of the major networks identified by (Wolovick et al., 2013), identified by the letters A-E, water flows uphill through the valley network and over topographic peaks (Fig 3d). As the water flows uphill, it freezes and releases latent heat (Fig 3c), warming the ice and maintaining the ice base at the melting point through otherwise cold-bedded regions (Fig 3b). In some cases (networks A and C), the water is used up by freezing and the network terminates, while in the others, freeze-on only consumes a fraction of the available water and the remainder continues downstream, eventually joining the water produced by local melting in the southeast corner of the domain. The southeast corner of the domain has few observations of basal water, but the deep ice there ensures that conditions are warm-bedded in the best-fit model. Overall, the model predicts a large amount of unobserved water in the deep valleys of the GSM. Either drilling to the bed or more advanced radar processing and analysis techniques would be needed to confirm whether these valleys do indeed contain unponded water.

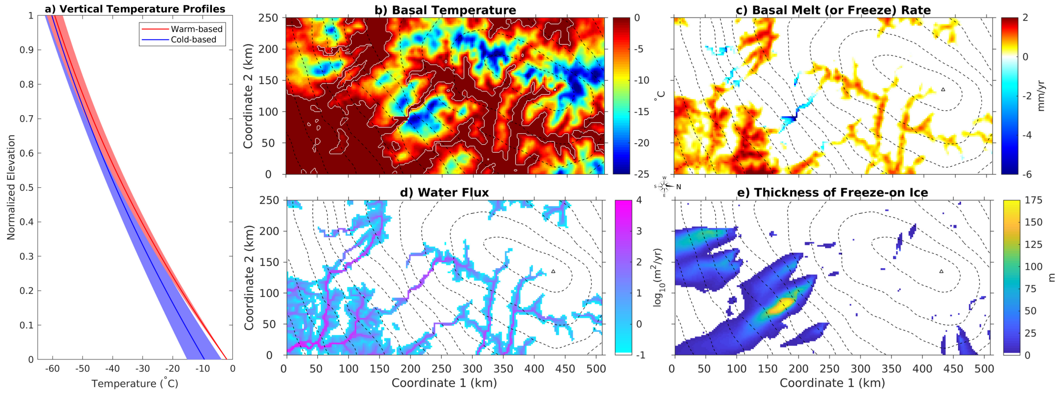

Figure 3. Thermal structure in the best-fit model. Panel a) shows vertical temperature profiles through the ice column. Profiles represent horizontal averages for warm-based and cold-based regions separately, and shading represents the standard deviation. Map plots show b) basal temperature, c) basal melt rate, d) basal water flux, and e) freeze-on thickness. Basal temperature in (b) has been corrected for the pressure dependence of the melting point and white line encloses the region at the melting point. Dashed lines show 50 m surface contours and triangle shows Kunlun station near the peak of Dome A. Letters A-E indicate major water networks and freeze-on plumes in observations.

Comparing our best-fit model results with the observational constraints allows us to verify the quality of our predicted thermal and hydrological structure. All of the major observed water networks are captured by the model (Fig 4b) with the exception of the uppermost reaches of network E (Fig 4c). The major freeze-on plumes are well-represented as well (Fig 5b), with most of the model freeze-on thickness falling in the "correctly located" category (Fig 5c). In fact, most of the incorrectly located model freeze-on appears to be edge effects around the margins of the correctly located freeze-on (Fig 5d). Whether because of artificial diffusion in the model advection scheme, or because of minor water routing errors in the freeze-on source regions, the model freeze-on plumes often extend more than one grid cell beyond the borders of the observed freeze-on plumes, leading to a penalty in the misfit function, most prominently at plume D. The model does not produce much freeze-on thickness in regions completely disconnected from the observed freeze-on plumes, giving us confidence that it is accurately representing the thermal state of the ice sheet as represented by the water and freeze-on observations. In addition, both the model produced by the evolutionary algorithm and the locally optimized model predict very similar distributions of basal temperature and freeze-on (not shown), giving us confidence in the robustness of our results.

Consistent with the results of our preliminary forward model tests, the freeze-on packages produced by these water networks in our model are smaller than their observed counterparts (Bell et al., 2011), generally achieving maximum thickness between 50-100 m, with only the freeze-on package produced by network D reaching 175 m (Fig 3d). However, the observed freeze-on unit at that location had a maximum thickness of nearly 1000m and a mean thickness of 400-500m. The observed freeze-on units are universally higher in the ice column than their modeled counterparts, despite the fact that the inversion tried to maximize freeze-on volume without any penalty for producing too much freeze-on at the observed locations. The inability of the model to produce larger freeze-on units is a fundamental consequence of the large latent heat of ice; it is simply not possible to remove latent heat fast enough to produce larger units in a steady-state model.

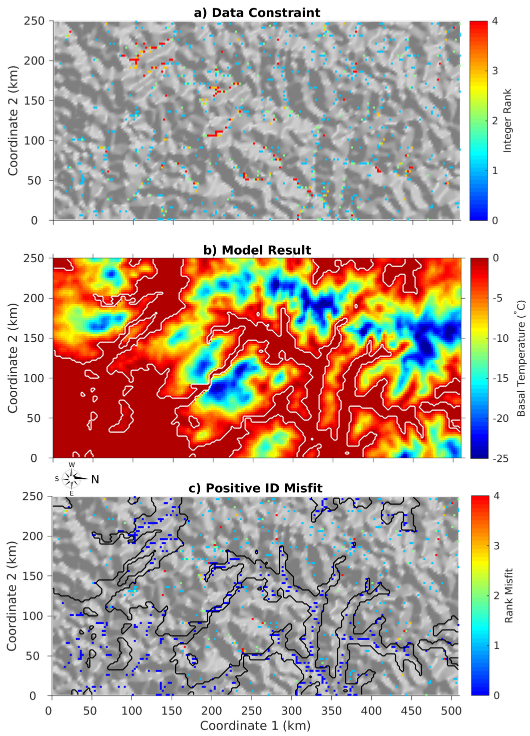

Figure 4. Best-fit model compared to the water constraint. a) Water observations overlain on hillshaded bed topography; b) model result for basal temperature relative to the melting point, with white contour enclosing region at the melting point; c) model misfit to the data plotted on top of hillshaded bed topography. Plot shows the severity of misfit for each observation; where the observed water falls within the model water (given by the black contour), the misfit is zero; where the observed water is not captured by the model, the misfit is given by the original confidence rank of the water observation.

We therefore interpret this discrepancy as evidence that additional processes intervene in reality to uplift freeze-on ice above the basal layer and into the mid-depths of the ice column. This represents a change in interpretation from Bell et al. (2011). They interpreted the radargrams to mean that the transparent ice below the observed freeze-on reflectors was composed of freeze-on ice; ie, the observed reflector represented the upper surface of an otherwise transparent package. We interpret the observed reflectors as representing the entirety of the freeze-on ice; ie, we interpret the observed reflector as representing volume scattering from impurities or sediment within the refrozen ice, with transparent and severely deformed meteoric ice below it. Additional processes not included in our model, such as time-variable basal slip (Wolovick et al., 2014; Wolovick & Creyts, 2016), small-scale rheological heterogeneity (NEEM Community Members, 2013), or complex flow patterns associated with the rugged topography of the GSM like viscous ice eddies (Meyer & Creyts, 2017), are then required to uplift the freeze-on ice several hundred meters above the bed and produce large englacial folds, where those are present.

2.2 Ice Sheet Flow Field

The vertical structure of the ice sheet flow field is marked by a strong concentration of shear in the lower 20-30% of the ice column, and nearly uniform velocity above that (Fig 6a). Though our model does not include basal sliding, the concentration of shear

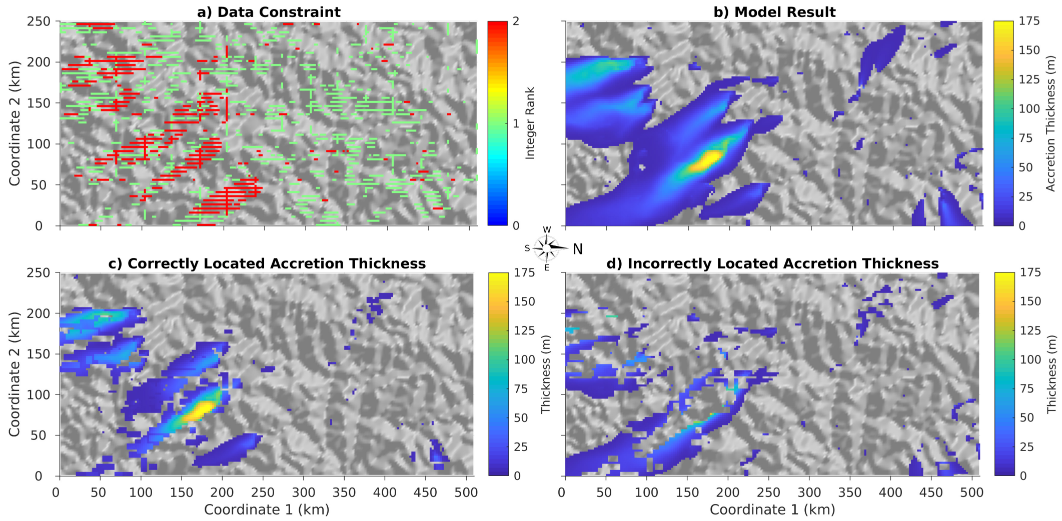

Figure 5. Best-fit model compared to the freeze-on constraint. a) Freeze-on observations overlain on hillshaded bed topography. b) Model result for freeze-on thickness. The color scale has been truncated where freeze-on thickness is less than 1 m and hillshaded bed topography is shown underneath. c) Correctly located freeze-on thickness, scaled by one half of the confidence rank of the observations at that location. The spatial integral of this field gives the "good" freeze-on volume in the positive ID misfit (Wolovick et al., (in review), Eq 15). d) Incorrectly located freeze-on thickness. The integral of this field gives the "bad" freeze-on volume in the negative ID misfit (Wolovick et al., (in review), Eq 16).

near the bed nonetheless increases in warm-bedded regions, as the increase in basal temperature also increases the rheological contrast with the colder and stiffer ice above (Fig 6a). In most of the domain, the upper 70-80% of the ice column is nearly rigid, moving downstream as a coherent unit while the warm soft layers underneath deform to accommodate the complex basal topography. This pattern is only broken in a narrow region near the divide, where a weak version of the Raymond effect (Raymond, 1983) causes deformation to spread out more evenly through the ice column (Fig 6a).

The horizontal structure of the ice sheet flow field follows from the governing assumptions of the balance flux algorithm we used to determine column-average velocity. Flow is slowest around the dome and increases with distance downstream, reaching a maximum of just over 3 ma^{-1} in the southeast corner of the domain (Fig 6a). While these velocities are very slow compared with rapidly sliding ice streams and outlet glaciers, the flow is nonetheless concentrated in narrow fingers of (relatively) faster-moving ice surrounded by slower-flowing areas. If this concentrated structure is real, it would continue the trend of "patterned enhanced flow" observed by Rignot et al. (2011) in areas of East Antarctica downstream of our model domain. The patterned flow that they observed was in ice moving several tens of ma^{-1}, about an order of magnitude faster than in our domain, but still well below the threshold of streaming flow. They attributed the patterned flow to basal sliding occurring even in slower-moving flank regions of the ice sheet, but our results suggest that basal slip is not necessary for flow to concentrate in tendril-like patterns. However, care should be taken in interpreting this aspect of our results. Our model uses a balance flux algorithm to compute ice flow, and balance flux algorithms make the simplifying assumption that the flow vector points exactly downhill (at least with respect to the smoothed ice surface). In reality there may be small angular deviations away from the perfect downhill direction, and spatial variations in the degree of

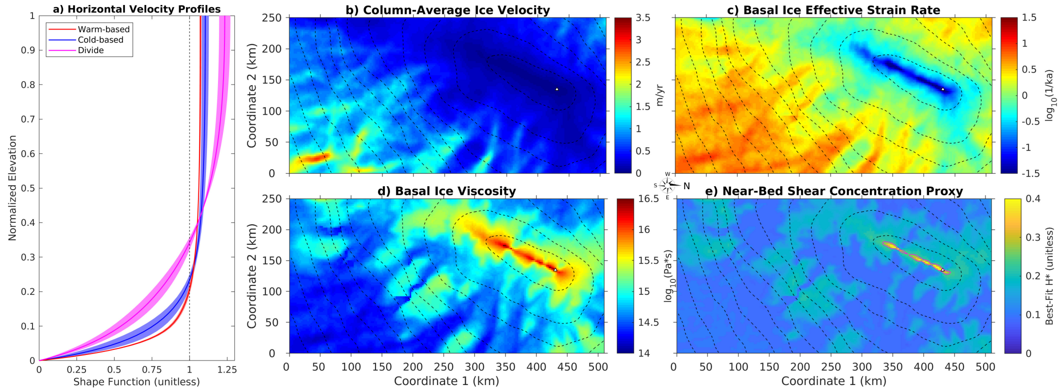

Figure 6. Flow structure in the best-fit model. Panel a) shows vertical profiles of the horizontal velocity shape function (ie, $\hat{u}$ from Wolovick et al., (in review), Eq 12). Profiles represent horizontal averages for warm-based, cold-based, and near-divide regions separately, and shading represents the standard deviation. Map plots show b) column-average velocity ($\bar{u}$), c) effective strain rate ($\dot{\epsilon}_E$) of the basal ice, d) basal ice viscosity (μ), and e) dimensionless corner elevation for best-fit D-J model (Dansgaard & Johnson, 1969). The corner elevation quantifies the degree to which shear is concentrated near the bed, with smaller values indicating that shear is more concentrated. The "near-divide" profiles in (a) are defined by corner elevation greater than 0.25, corresponding to areas within the purple contour in (e). Dashed lines show 50 m surface contours and triangle shows Kunlun station near the peak of Dome A.

longitudinal coupling will also produce variability in the appropriate horizontal averaging scale over which "downhill" ought to be defined. These small deviations from the assumed downhill direction can become magnified during the balance flux integration, potentially producing erroneous structure in the model velocity field.

Regardless of whether the tendrils of relatively faster flow away from the dome are accurate, the slow flow and weak Raymond effect near the dome are a robust result of our model. The ice surface forms a divide ridge for about 100km south and to the east of the peak of Dome A, a geometry known to give rise to the Raymond effect. The Raymond effect (Raymond, 1983) is the phenomenon whereby the non-Newtonian rheology of ice combines with the very low rates of vertical shear underneath a divide to produce a core of stiff ice near the bed, thus resisting vertical thinning and causing the upwarping of internal layers. The Raymond effect is strongest in an isothermal ice sheet which is frozen to a flat bed. In Dome A, the Raymond effect is weakened by topographic variability in the bed and by the extreme thermal contrast between the bed and the surface. This thermal contrast- approximately 60°C- ensures that the ice near the bed remains softer than the ice near the surface regardless of the strain rate, while the large-amplitude variability in the subglacial mountains ensures that the dominant signal in the internal layers is always going to be draping over the topography. Nonetheless, strain rates are substantially lower at the bed underneath the divide than they are at the bed on the flanks (Fig 6b), and this leads the basal ice to be stiffer there than it is away from the divide (Fig 6c), producing more distributed shear within the ice column (Fig 6a). We can quantify the impact that this (relative) basal stiffening has on the englacial velocity distribution by fitting a best-fit Dansgaard-Johnson (D-J) model (Dansgaard & Johnson, 1969) to the shape function for horizontal velocity. A D-J model approximates the horizontal velocity field with a piecewise linear function of depth, where the velocity increases linearly from the bed up to a corner elevation H*, and is constant above that. The best-fit value of H* thus provides a convenient way to quantify the degree to which shear is

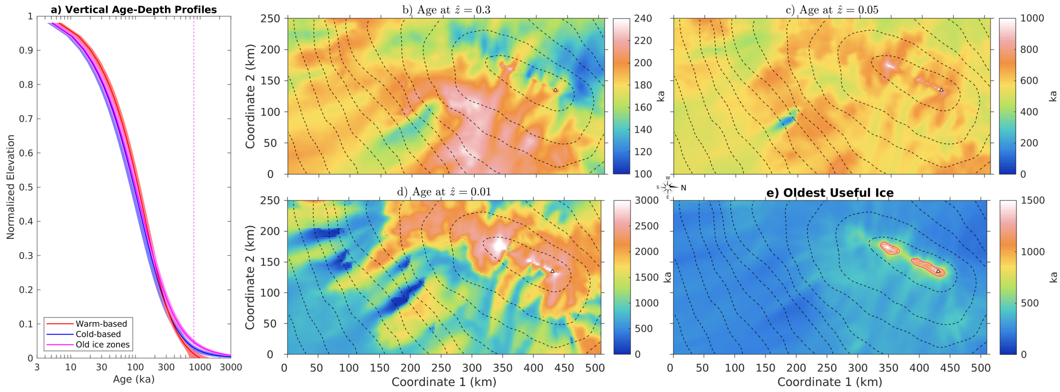

Figure 7. Age structure in the best-fit model. Panel a) shows vertical profiles of the age-depth scale. Profiles represent horizontal averages for warm-based, cold-based, and old-ice regions separately, and shading represents the standard deviation. Mean and standard deviation were both computed on a logarithmic scale, and only meteoric ice was included in the calculation. Map plots show ice age at normalized elevations of b) 30% ice thickness, c) 5% ice thickness, d) 1% ice thickness, and d) oldest useful ice for paleoclimate records. The oldest useful ice is computed using an accumulated shear steepening function that measures the likelihood that small stratigraphic perturbations will overturn, as well as a maximum temporal smoothing due to isotopic diffusion of 10 ka. Note changes in color scale between each map panel. "Old-ice regions" in panel (a) defined by areas with oldest useful ice greater than 800 ka, marked by the red contour in (e). The 800 ka threshold was chosen to correspond to the oldest ice in the EPICA Dome C ice core (Jouzel et al., 2007). Dashed lines show 50 m surface contours and triangle shows Kunlun station near the peak of Dome A.

concentrated near the bed. While the best-fit H* is less than 20% of the ice thickness in the vast majority of the domain, we can see it rise to about 40% of ice thickness underneath the divide (Fig 6a,e), reflecting a flow regime in which shear is less concentrated near the bed, a hallmark of the Raymond effect. As we will show next, this weak Raymond effect has profound consequences for the age structure of the ice sheet.

2.3 Age Structure and Internal Layers

The age-depth profile of the ice sheet shows relatively weak spatial variability at mid-depths, with profiles that increasingly diverge near the bed (Fig 7a). If we take a horizontal slice at 30% of the ice thickness (ie, roughly at the top of the basal shear layer; c.f. Fig 6a), we see that the age structure of the ice sheet is dominated by the twin influences of basal topography and horizontal advection (Fig 7b). In broad subglacial valleys, the characteristic vertical strain rate (defined by the ratio of accumulation rate to ice thickness) is smaller, producing older ice at similar positions within the ice column. Conversely, subglacial peaks produce a larger characteristic strain rate and younger ice. This phenomenon can also be seen in the way that warm-bedded regions have older ice than cold-bedded regions at mid-depths in Fig 7a. However, this effect of the local vertical strain rate is modified by the presence of horizontal advection: downstream of prominent peaks, especially around (200,100), we can see streaks of younger ice, while prominent valleys produce downstream streaks of older ice. The greatest degree of short-wavelength spatial variability in the mid-depth layers can be seen underneath the divide, where slow flow diminishes the importance of horizontal advection, while away from the divide the age structure of the ice sheet is much more smoothed out. However, the situation reverses near the bed. At normalized elevations of 5% and 1% (corresponding to average elevations of 125 and 25 m above the bed, respectively), the youngest ice is found in the valleys and the oldest ice on the peaks (Fig 7c,d). This is due to basal melting destroying older ice within the valleys, and causing the age-depth profiles to intersect the bed at finite age (Fig 7a). In addition, very young ice can be found above the freeze-on regions (Fig 7c,d; c.f. Fig 3e), where the "age" in this case represents time since freeze-on rather than time since surface deposition. The oldest ice is found in a thin region underneath the divide corresponding to the weak Raymond effect discussed in the previous section. At 1% elevation, ice older than 2 Ma is widespread and ice older than 3 Ma can be found as well (Fig 7d). The oldest ice is found underneath the divide, with a gap corresponding to a basal valley in which basal melt occurs (Fig 7d, c.f. Fig 3b,c).

However, just because extremely old ice is present does not mean that is is necessarily useful to ice coring. To obtain a useful climate record from an ice core, the ice must both be in stratigraphic order and it must not have been thinned so much that useful temporal resolution has been lost. To estimate the oldest useful ice in the model, we used thresholds reflecting both of these criteria. For our stratigraphic continuity threshold, we know that vertical shear increases the likelihood that small stratigraphic perturbations will steepen and overturn (Waddington et al., 2001; Jacobson & Waddington, 2004, 2005); while we cannot resolve these small perturbations in our large-scale model, we can resolve the vertical shear, so we computed an accumulated shear steepening index to estimate the likelihood of small-scale overturning. This steepening index can be thought of as finite-amplitude rotation in a vertical plane; beginning from zero when the ice is deposited at the surface, it accumulates along particle paths and grows most rapidly when vertical shear exceeds vertical thinning. Because we cannot resolve small-scale layer overturn in our model, we do not know a piori what value of the steepening index to use as our threshold; so we empirically estimate a threshold value by comparing our model to the observed height of the echo-free zone (EFZ), the region near the bed in radar echograms where smooth continuous stratigraphy is no longer observed. The observed EFZ varies between 4% of the ice thickness under the divide (where the picks may be too high owing to the difficulty in detecting continuous layers close to a variable bed reflector) to a maximum of 38% of the ice thickness, with a mean value of 18% of the ice thickness. The best-fit threshold produces an RMS misfit with respect to the observed EFZ of 4% of the ice thickness, which we consider to be acceptable. For our layer thickness threshold, we assumed that the limiting factor would be isotopic diffusion rather than analytical equipment, on the argument that technology can always improve the spatial resolution possible at ice core laboratories, but that no technological improvements can reverse the loss of information due to diffusion. Many authors have computed isotopic diffusion using a simple $\sqrt{\kappa t}$ scaling, however the diffusion coefficient κ is temperature-dependent and varies by over three orders of magnitude as the ice layers descend from the surface to the bed. We therefore computed the characteristic spreading length of an impulsive isotopic perturbation as follows,

$$\frac{D\sigma}{Dt} = \frac{\kappa}{\sigma}, \tag{1}$$

where σ is the characteristic spreading length perpendicular to the layers, $\frac{D}{Dt}$ is the material derivative, and κ is an Arrhenius function of temperature. The boundary conditions are that σ is zero at the surface and bed. To derive the above equation, we assumed that an initial delta-function isotopic perturbation would spread out perpendicular to the locally planar layers with a Gaussian shape with a standard deviation given by σ. We solved for the steady-state σ field using the same advection solver used for the rest of the model, computed the layer thickness directly from the vertical gradient of the age field, and then conservatively took the ratio of 2σ over the layer thickness to represent the finest temporal resolution that could be achieved before diffusion smoothed out climate signals. To compute the oldest useful ice we assumed that the coarsest useful temporal resolution would be 10ka, such that the Nyquist frequency would catch the precession cycle at about 20ka, while the important obliquity cycle would have 4 samples per cycle.

Using these steepening and layer thickness thresholds, we were able to estimate the oldest useful ice (Fig 7e). While in most of the domain intense vertical shear in the lower quarter of the ice column ensures that it would be difficult to obtain an intact climate record extending more than a few hundred thousand years into the past, underneath the divide the situation is different. There are two distinct patches of extremely old ice underneath the divide where useful ice older than 1 Ma can be expected, and in fact our model predicts that useful ice up to 1.5 Ma may be present as well, a key finding as locating a continuous ice core record back to 1.5 Ma has been identified as an important target for understanding the climate of the Quaternary (Fischer et al., 2013). These two patches are elongated in the direction of the ice surface ridge; the larger of the two contains the present-day ice peak while the smaller patch is centered around a small subsidiary peak in the ice surface topography. So long as the position of the ice divide has remained stable over time, both of these two patches are likely to contain extremely old ice in stratigraphic order.

It is therefore important to explore what the results of our inversion can say about the history of divide migration around Dome A. The pattern of accumulation rate resolved by the inverse model displays a precipitation shadow effect associated with the ice sheet surface topography. We plot surface elevation contours in Fig 2b to facilitate this comparison: to the northwest of the ice divide (ie, in the direction leading towards Lambert Glacier, the Amery Ice Shelf, and the ocean), we can see the highest accumulation rates in the domain, about 24 mm a^{-1}. Meanwhile, to the southeast of the divide (ie, on the side facing the ice sheet interior) there is a pattern of lower accumulation subparallel to the ice divide, about 15-17 mm a^{-1}, and two additional local minima (down to $\sim$14 mm a^{-1}) located on the inland side of the divide as well. Furthermore, this precipitation shadow is located within the center of the model domain, where errors are low (Fig 2d). Thus, while we do not have confidence in structure produced by the inversion near the edges of the domain, we do have confidence that the precipitation shadow associated with ice surface topography is robust. Since these results represent a steady-state accumulution rate field averaged over the last 161 ka (the age of the oldest dated layer used in our inversion), they imply that the precipitation shadow created by the modern-day ice sheet topography has been stable for at least one and a half glacial cycles. A stable precipitation shadow would argue against large-scale divide migration. Our results do not have sufficient precision to rule out small-scale divide migration, on the order of 50 km in the across-divide direction. In addition, we would probably not see much difference in our results if the peak of Dome A migrated up and down the present-day ridge over time (Fig 1a). However, large-scale migration, such as a jump from the present-day ice divide which is anchored on the northern spur of the GSM to an alternate ice divide which is anchored on the southern spur of the mountains (Fig 1b), can be ruled out, at least within the last one and a half glacial cycles.

A detailed look at the fit between the modelled and observed internal layers (Fig 8) does not provide evidence for divide migration either. The precipitation shadow pattern is clearly visible in the raw data for all layers (Fig 8a,d,g,j,m), where it is manifested as higher layers (redder colors) on the southeast side of the ridge and lower layers (blue colors) on the northwest side. The model captures the long-wavelength spatial structure of the observed layers quite well, although the observed layers generally have more short-wavelength variability than the model. The misfits for the dated layers (Fig 8c,f,i,l) are dominated by a temporal pattern in which the model layers are systematically too high in the ice column for the younger layers (38 and 48 ka; Fig 8c,f) and systematically too low in the ice column for the older layers (90 and 161 ka; Fig 8i,l). This temporal pattern is explained by the fact that the steady state model is solving for a temporally av-

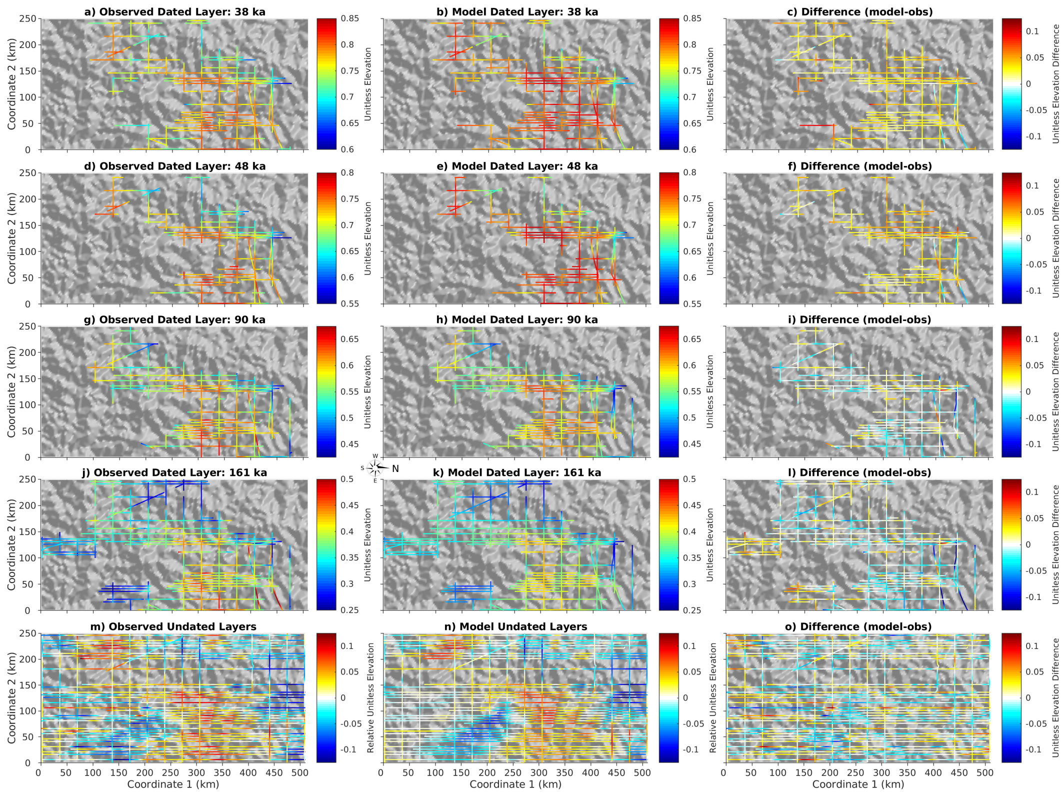

Figure 8. Best-fit model compared to the internal layer observations. Left-hand column (a,d,g,j,m) shows the observed dated and undated layers; middle column (b,e,h,k,n) shows the corresponding model layers; right-hand column (c,f,i,l,o) shows the difference, positive when the model layer is higher in the ice column. Each row represents a particular layer (38 ka, 48 ka, 90 ka, 161 ka, and undated). For the dated layers, the model layer is the taken to be the isochron with the corresponding age, while for the undated layers, the model isochron selected for comparison is the isochron that best matches the average depth of the observed layer. Thus, the undated layers (m,n,o) are only sensitive to spatial gradients in layer depth rather than the absolute value of depth. Hillshaded bed topography is shown in the background of all plots.

eraged accumulation rate: if accumulation is higher during interglacials, then more recent layers should be pushed down lower in the ice column than would be implied by the temporally averaged accumulation rate, while older layers should respond more to the lower accumulation rate during glacial periods and thus be higher in the ice column. The spatial patterns in the misfit do not appear to be correlated with the precipitation shadow. The largest misfit values for the undated layers are seen near the freeze-on associated with network D, where unresolved small-scale deformation processes produce large englacial folds not captured by the model. Outside of this location, the magnitude of the layer depth misfit is generally on the order of 5% of the ice thickness or less.

3 Discussion

3.1 Ice Cores and Old Ice

Our model strongly suggests that the ice divide extending southwest of Dome A is a promising location to drill an old ice core, with two distinct regions of very old ice found near the bed along this ridge (Fig 7). The reasons for this are straightforward and robust. Our model includes all of the terms in the strain rate tensor when computing ice viscosity, even if it does not compute the full stress balance (Wolovick et al., in review). It therefore includes a simplified representation of the mechanism behind the Raymond effect, which brings old ice layers closer to the surface underneath ice divides (Raymond, 1983). Our model also accounts for the temperature effect on rheology, which weakens the Raymond effect when ice near the bed is warmer and therefore softer than ice near the surface. A classic Raymond arch may not be visible in the stratigraphy underneath Dome A (Zhao et al., 2018; Wang et al., 2018) owing to the twin effects of thermal weakening and topographic draping, but the prediction that a weak Raymond effect should nonetheless be present is a simple consequence of the divide geometry and ice rheology. In addition, vertical shear in flank positions, magnified by ice flow over a highly variable bed, should cause small perturbations to overturn in the lower portion of the ice column, producing the echo-free zone. In some cases, we can even observe small-scale folding in the radar data as the upper boundary of the echo-free zone eats into the overlying smooth stratigraphy (not shown). Under the divide, this vertical shear should be greatly reduced, producing an environment much more conducive to stratigraphic continuity. Our prediction that extremely old ice in stratigraphic order may be found underneath the ice divide (with small gaps corresponding to deep valleys where melting occurs) is thus a robust consequence of the divide geometry itself.

The one major complication to this generally hopeful picture for ice coring is the potential for divide migration. Our model predicts that regions off of the divide should experience a large amount of vertical shear, and thus small stratigraphic perturbations are likely to overturn. Thus, if the old-ice patches were once in a flank regime, their layers would probably be disturbed. However, the present-day ice divide is aligned with a prominent ridge in the underlying mountains (Fig 1a,b), and it is reasonable to assume that the subglacial mountains stabilize the position of the ice divide. Under this hypothesis, it would take a large change in forcing (most likely far-field changes in surface slope and ice flux that diffuse inland from the coast; see Gillet-Chaulet & Hindmarsh (2011) for detailed discussion of the influence of far-field forcing on ice divide geometry) to cause the ice divide to jump to a different stable position, such as the high basal topography on the southern spur of the GSM (Fig 1b). The fact that our inverted accumulation rate contains a precipitation shadow pattern aligned with the present-day divide (and the fact that this pattern is seen in the raw layer data as well) gives us confidence that the ice divide has not made this jump within the last one and a half glacial cycles. In addition, the observed freeze-on reflectors are continuous for 100-150 km downstream of their source regions (Fig 5a), which implies stability in both the ice flow direction and their freezing source regions for roughly 100-150 ka. Large-scale divide migration would interrupt the continuity of the observed freeze-on reflectors by both changing the ice flow direction and by removing the surface gradient that drives water uphill into their freezing source regions. Of course, we cannot rule out earlier migrations before the earliest dated layer and freeze-on reflector used in our inversion, but we expect the glacial-interglacial cycle to be the largest forcing change experienced by the ice sheet in the recent geologic past, so the fact that the divide made it through a complete cycle without migrating is a hopeful sign for its stability in the longer term.

However, while our model may rule out large-scale divide migration in the last one and a half glacial cycles, and while we may be hopeful that this result also indicates a lack of large-scale migration in previous cycles, that still leaves open the possibility that stratigraphic continuity could have been disturbed by small-scale divide migration. The ice divide could migrate $\sim$50 km or less in the northwest direction and remain roughly positioned over the northern spur of the GSM (Fig 1a,b). None of the arguments against large-scale migration that we advanced above apply to small-scale migration: such a migration would be small enough that it would still be consistent with the hypothesis that divide position is stabilized by subglacial topography; our inversion has a course enough resolution that we would probably not be able to distinguish the resulting precipitation shadow from one caused by the modern surface topography; and the ice flow and hydrologic routing in the vicinity of the freeze-on regions would probably remain roughly the same. Yet such a migration would put our putative old ice patches temporarily in a flank regime, where they would be vulnerable to stratigraphic overturn due to vertical shear. Fortunately, stratigraphic overturn would not be guaranteed in this scenario. The rotation rate of layer perturbations is proportional to the horizontal velocity of the ice sheet, and such small divide migrations would still leave our old ice patches in a region of slow flow near the divide (Fig 6b), so it is possible that stratigraphic continuity could survive if the divide excursion was more rapid than the overturn time. More detailed dynamic modeling is needed to determine the duration and magnitude of small divide excursions, and whether those excursions would be sufficient to cause stratigraphic overturn.

But even assuming a stable ice divide, it would be inappropriate to use our model to choose a specific drilling location. This is due both to processes which we leave out of the model, and to the inherent deficiencies of a gridded bed map in a region with a large degree of topographic variability. The two biggest omissions from our model as it relates to old ice is the lack of a full stress balance and the lack of an anisotropic rheology. Near the divide, the shallow ice approximation becomes a poor representation of the ice sheet stress state. When surface gradients are very low and flow is very slow, the stress regime becomes dominated by far-field horizontal stresses rather than vertical shear. While we did include the full strain rate tensor in our viscosity computation (Wolovick et al., in review), that is not the same as solving the Full Stokes equations for the ice flow, or allowing the flow vector to deviate from the assumed downhill direction. Furthermore, near a divide the ice can develop a preferential crystal orientation fabric, which produces an anisotropic rheology that can have major impacts on the age-depth scale, especially near the bed (Zhao et al., 2018). Finally, even if we had run a Full Stokes model with an anisotropic rheology, our model would still have been limited by the incomplete nature of the gridded topography.

3.2 Unresolved Basal Topography

The GSM underneath Dome A contain an enormous degree of short-wavelength topographic variability, and a large portion of this variability is not captured by BEDMAP2 (Fig 9). The gridded topography cannot capture this short-wavelength variability for two reasons: 1) the AGAP flight line spacing is 5 km, so content at shorter wavelengths than that cannot be represented even with a perfect gridding algorithm; and, 2) the actual gridding algorithm used must make compromises between regions with sparse data coverage, where greater spatial smoothing is appropriate, and regions with dense data coverage like the GSM, where less spatial smoothing would have been better. Local deviations from the gridded topography are largest in the northwest of the domain, reaching RMS values of $\sim$250 m (Fig 9c), and smallest in the southeast corner, where they drop to 130 m. Individual peaks and valleys often differ from the gridded topography by double the RMS value. A close examination of the along-track radar data reveals that numerous short-wavelength valleys with aspect ratios of around 1/5 (depth over width) are ubiquitous, and a few valleys with aspect ratios up to 1/3 or even slightly higher can be found as well.

None of these short-wavelength topographic features are included in the smooth gridded topography, but all of them would have important effects on the local ice flow in their vicinity. In a strongly shearing flank flow regime, these short-wavelength topographic features should promote complex folds and stratigraphic overturn near the bed, and some of the narrower and deeper valleys may even host viscous ice eddies with counterflow at the base (Meyer & Creyts, 2017). In the divide flow regime, the lack of strong vertical shear means that these short-wavelength valleys and mountains are unlikely to cause overturning, but they should still play a strong role in modifying the flow and de-

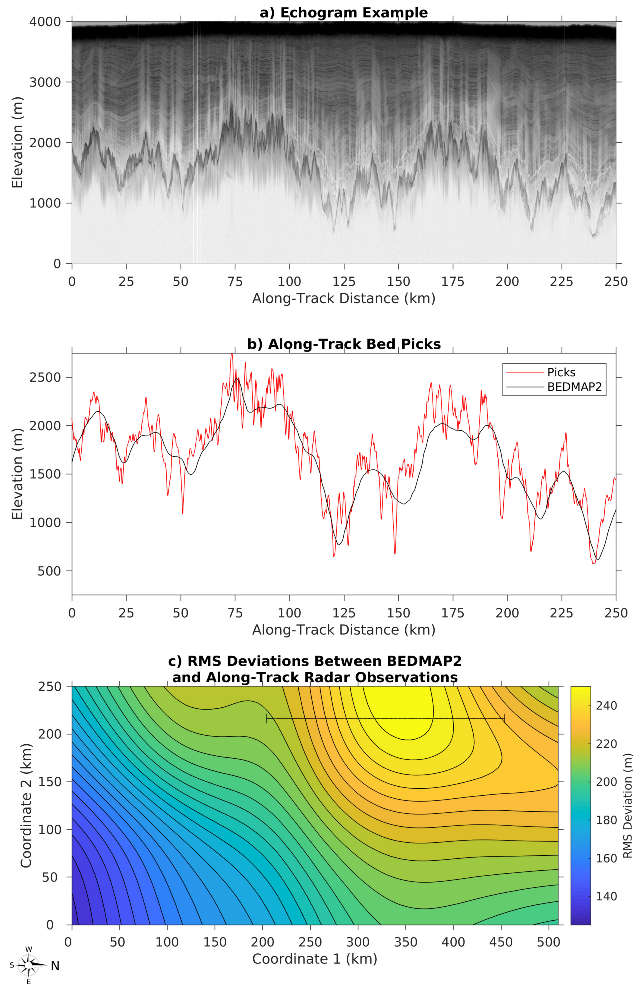

Figure 9. Short-wavelength deviations between bed topography measured along-track and gridded bed topography in BEDMAP2. a) Example echogram featuring copious topographic variability. b) Bed picks for the echogram in (a) with BEDMAP2 bed elevation overlain. c) Map of RMS deviations between gridded topography and true topography measured along-track. The "mean" stage of the RMS calculation was performed with a gaussian weighting function with a 50 km standard deviation ($\sim$100 km wavelength). Horizontal line shows the location of the example echogram.

formation regime of the ice near the bed. Our large-scale model is sufficient to make a broad-scale prediction that there are two promising old ice patches aligned with the divide, but any attempt to predict the precise details of the age-depth scale would need to resolve this short-wavelength topography and the effect that it has on ice flow. Closely spaced survey lines along the whole length of the divide- on the order of 500 m to 1 km apart, for the entire 100 km long divide- are an essential prerequisite to any attempt to predict the location of the oldest ice in detail. Furthermore, this unresolved short-wavelength topography is likely to have an effect on the ice sheet thermal structure, which will in turn lead to a bias in our inverted geothermal flux estimate, which we try to estimate below.

3.3 Estimating Geothermal Flux Bias

Our geothermal flux estimates are higher than all of the prominent prior estimates for this region (Shapiro & Ritzwoller, 2004; Fox-Maule et al., 2005; An et al., 2015; Martos et al., 2017). Fundamentally, our high estimates are being driven by the observations of subglacial water. The observations demand that subglacial water be present in the model both directly, through the water constraint, and indirectly, through the requirement that liquid water must exist at the ice sheet base in order to produce freeze-on plumes matching the freeze-on constraint. However, the ice sheet thermal state is heavily dependent on ice thickness. Thicker ice provides better insulation from the cold surface temperatures, encouraging warmer conditions, while thinner ice increases the rate of conductive cooling, encouraging colder conditions. Thus, deviations between the gridded ice thickness and the true ice thickness have the potential to change the thermal state of the bed. If the observations demand water at a particular location, but the model ice thickness is too low, then the model will compensate by making the geothermal flux higher than it should be in order to ensure that the bed is still warm. Because subglacial water is preferentially located in topographic minima, this effect will produce a systematic bias in our inferred geothermal flux estimate, since the real subglacial water bodies are located in narrow valleys which are not fully resolved by the smoothed grid.

We can estimate this bias by looking at the mismatch between the gridded topography used as a model input and the true topography measured along-track in the radar data at the locations of the observed water bodies. To do this, we first constructed a smoothed estimate of the ice thickness bias between the water observations and the gridded topography (Fig 10a). This estimate is different from the RMS estimate we presented previously (Fig 9c) because we are only interested in the deviations at the locations of the observed water. We computed this estimate by first computing the difference between the along-track radar measurements of ice thickness at the locations of the water observations and the corresponding gridded value, and then constructing a weighted average based on the observational confidence (Fig 4a) and a Gaussian distance weighting with the same 50 km standard deviation (100 km wavelength) as the rest of the inversion. Next, we computed a smoothed ice thickness product at the same wavelength, and used that smoothed ice thickness product both to normalize the ice thickness bias (Fig 10b) and to compute a characteristic conductive heat flux under the assumption that the bed is tied to the melting point everywhere (Fig 10c). The product of those two quantities then represents the bias in conductive heat flux (Fig 10d). Since this bias in conductive heat flux should only affect our inversion results when either the water or freeze-on observations are responsible for setting the lower bound on geothermal flux, we then computed the combined contribution of those two data types to setting the lower bound (Fig 10e). Finally, we estimated the bias in geothermal flux (Fig 10f) by taking the product of that contribution with the bias in conductive heat flux. We show our final bias-corrected estimate of geothermal flux in Fig 10g. We assume that there is a 50% uncertainty in the above procedure for estimating the geothermal flux bias, and we add this error to our previous estimate of geothermal flux uncertainty (Fig 2c) in quadrature to produce our final uncertainty estimate for geothermal flux (Fig 10h).

With a mean value of 4.5 mW m^{-2}, this estimated bias accounts for most of the 5.4 mW m^{-2} mean difference between our geothermal flux results and those of Martos et al. (2017). Given that our estimate of this bias was only approximate, and given that a proper estimate of this bias would require a high-resolution model using a high-resolution topographic grid as input (with a high-resolution field survey necessary to produce that grid), we interpret our bias-corrected results as being consistent with Martos et al. (2017), at least in a spatially averaged sense.

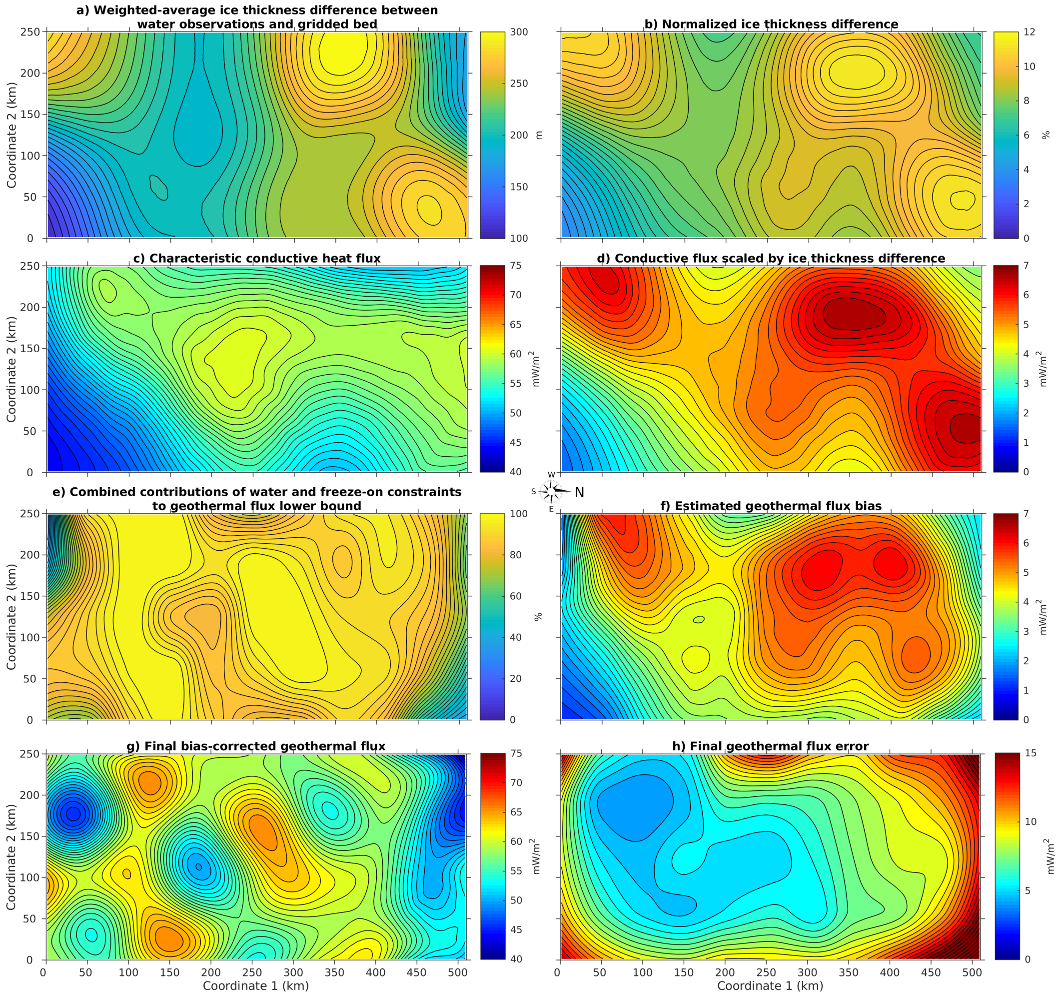

Figure 10. Bias estimation for geothermal flux. a) Offset between ice thickness at the along-track locations of the water observations and the corresponding ice thickness in the gridded topography, weighted by observation confidence (Fig 4a) and spatially smoothed; b) the same quantity, normalized by smoothed ice thickness; c) characteristic conductive heat flux; d) conductive heat flux scaled by ice thickness offset (ie, the product of (b) and (c)); e) combined contributions of water and freeze-on observations towards constraining the lower bound on geothermal flux in the inversion; f) our estimate of the bias in our inverted geothermal flux (the product of (d) and (e)); g) our final bias-corrected geothermal flux estimate (ie, Fig 2a minus (f)); and h) the uncertainty in our final estimate of geothermal flux.

3.4 East Antarctic Geology

Nevertheless, our inversion has revealed that geothermal flux in the GSM may well be higher than previously believed, especially in localized regions. While the mean offset between our results and the Martos estimate may be explained by the thermal effect of unresolved narrow valleys, the Martos estimate was itself on the high end of previously published geothermal flux estimates for this region. Other prominent estimates put the mean geothermal flux in our domain at 47 mW m^{-2} (An et al., 2015), 48 mW m^{-2} (Shapiro & Ritzwoller, 2004), or 53 mW m^{-2} (Fox-Maule et al., 2005). In contrast, the Martos estimate- which was the only one of the previous estimates to be constrained by local aeromagnetic data- put the mean heat flow in our domain at 57 mW m^{-2}. Our bias-corrected estimate puts the mean heat flow at 58 mW m^{-2}, with local excursions up to 66 mW m^{-2} (prior to bias correction, these figures were 62 and 72 mW m^{-2}, respectively). Thus, our inversion suggests that heat flow in the GSM may be closer to the global continental average (65 mW m^{-2}, (Jaupart & Mareschal, 2007)) than to values typical of Proterozoic continental cratons (48 mW m^{-2}, (Jaupart & Mareschal, 2007)).

Furthermore, our inverted geothermal flux would have been even higher had we not included the Martos estimate in our cost function. In our companion paper (Wolovick et al., in review) we quantitatively attributed our inversion results to each of the misfit components: in two thirds of the domain, the Martos aeromagnetic model is responsible for 75% or more of the misfit increase at the upper bound on geothermal flux. Only in a few locations- most prominently in the freeze-on plume at the terminus of network A- does the freeze-on constraint provide a meaningful upper bound on geothermal flux. In the rest of the domain, the radar data are responsible for setting the lower bound on geothermal flux, not the upper bound. This is significant because the bias in our geothermal flux estimate arising from the presence of narrow unresolved valleys is really a bias in the lower bound only: deep subglacial valleys make it *possible* to have subglacial water at a lower geothermal flux than would be possible in shallower valleys; but of course the deep valleys will still have subglacial water if the geothermal flux is higher as well. Without the aeromagnetic constraint, the upper bound of our geothermal flux estimate would be unconstrained in a large fraction of the domain. In effect, by including the Martos estimate we gave the conventional wisdom about East Antarctic geology a 20% stake in our misfit function. If we had not credited the conventional wisdom in this way, our estimate would have been much higher.

Our inversion has also revealed a large degree of spatial variability in geothermal flux that was not known before. The basic pattern of spatial variability we found remains the same both before and after bias correction (Fig 2a, c.f. Fig 10g). The highest values still occur in the catchment region of water network A (Fig 10g, c.f. Fig 3). All of the major water networks are still associated with dipole patterns in geothermal flux, with higher values found in their upstream catchments and lower values found near the freezing zones at their termini. This sort of spatial variability should be expected in geothermal flux; indeed, had our inverse model allowed structure at smaller wavelengths, we likely would have resolved even more variability. In places where it can be more easily measured on land, geothermal flux is known to have a high degree of spatial heterogeneity, even in old continental cratons (Jaupart & Mareschal, 2007). Differences in tectonic, magmatic, and hydrothermal history, and differences in the distribution of radioactive elements within the crust, all combine to produce a great deal of local variability in continental heat flow. Even within the population of Proterozoic cratons, heat flow varies: while the mean of this class of continental crust may be only 48 mW m^{-2}, individual cratons may be as high as 90 mW m^{-2} or as low as 36 mW m^{-2} (Jaupart & Mareschal, 2007, Table 3). The Shapiro & Ritzwoller (2004) estimates of heat flow may have been the lowest in our domain, but even they were explicit that the "error" estimate they provided was actually an estimate of the local spatial variability that should be expected about their central value. Our results do not contradict the conventional wisdom that

East Antarctica is an old Proterozoic continental craton. They do, however, challenge the frequently unexamined corollary that its heat flow must therefore be uniformly low. Variability at all spatial scales is a central feature of geothermal flux measurements. Some old cratons have quite high heat flow, while others are very low. A similar degree of variability in East Antarctica should be the expectation, not a surprise.

Ice sheet modelers typically ignore the potential for spatial variability in geothermal flux, since we usually lack the means to constrain it; but the basal hydrology and thermal structure of the ice sheet will respond to this variability nonetheless. While we cannot speak with specificity about the pattern of geothermal flux outside of our domain, we can make general inferences about how we expert the thermal structure of the ice sheet and bed to behave. First of all, we expect basal hydrology to redistribute latent heat underneath the ice sheets, so that cold regions downstream of melting zones will be warmer than they otherwise would be. Ice sheet thermal models without basal hydrology and freeze-on will underestimate basal temperatures downstream of melting zones, especially along narrow hydrological flow paths. Secondly, we expect to see more heterogeneity in the basal thermal state than would be implied by spatially smoothed estimates of geothermal flux. For example, one often-cited study of Antarctic basal temperatures (Pattyn, 2010) ran sensitivity tests with multiple geothermal flux maps, but all of the maps that they tested were course-resolution products with ad hoc localized adjustments to account for radar observations of subglacial lakes. As a result, they predicted that large swaths of the Antarctic ice sheet are basically guaranteed to be warm-bedded, and that the melt rate in these regions ought to be uniformly positive. In reality, there are likely to be numerous local variations in basal temperature, and even within regions that are uniformly warm-based, there are likely to be local transitions between melting and freezing conditions. The ice sheet base is probably a hodgepoge of conditions: cold-based, warm-based but freezing, and warm-based melting. This variability is consistent with observed 10 km-scale variability in basal morphology (Bingham et al., 2017), which also acts as a driver for the water routing system. The expectation of heterogeneity ought to inform our interpretation of the geomorphic and detrital record of past ice sheet dynamics, and also our interpretation of model results for present-day ice sheets. When interpreting the results of ice sheet thermal models, we should keep in mind that, while thermal uniformity may be a technically correct result given smooth boundary conditions used as model input, in reality we expect the ice sheet base to be heterogeneous.

4 Conclusions

We have used a formal inverse model to assimilate radar observations of subglacial water, freeze-on, and internal layers into a thermomechanical model of the ice sheet and basal hydrology around Dome A in East Antarctica. Using this inverse model, we have estimated the geothermal flux and long-term accumulation rate boundary conditions acting on the ice sheet over the last 161 ka. Based on those boundary conditions, we were able to produce a self-consistent estimate of the ice sheet flow field, thermal structure, and basal water flow informed by those observations.

Our inferred distribution of basal water and freeze-on largely matches the observations, but the use of a self-consistent physical model allows us to constrain melt rates and freeze-on volumes. We find that it is unlikely that the full thickness underneath the reflectors identified by Bell et al. (2011) is composed of freeze-on; instead, a change of interpretation is warranted, such that the observed reflectors likely reflect volume scattering from within the body of the freeze-on unit, with transparent meteoric ice underneath. We also predict a large amount of basal water in the trunk valleys of the GSM. While this water does not appear to be ponded in the same way as the clear subglacial lakes in the networks identified by Wolovick et al. (2013), it is likely that a large volume of subglacial water flows down these valleys and out towards downstream regions of the ice sheet. This prediction could be tested by drilling to the bed, by more advanced radar techniques, or by active source seismic surveys.

Our inferred accumulation rate field contains a precipitation shadow pattern aligned with the modern-day ice divide, suggesting that there has not been any large-scale divide migration in the last one and a half glacial cycles. The same pattern also appears in the raw layer data used to constrain the model, giving us added confidence in its validity. The continuity of the observed freeze-on units also argues against large-scale divide migration within the last glacial cycle. While we cannot say anything with certainty about divide migrations in previous cycles, the fact that the divide went through a full glacial cycle's worth of forcing changes without large-scale migration is a hopeful sign for divide stability in the longer term. If the divide has indeed been stable on longer timescales, then our model predicts that extremely old ice- perhaps up to 1.5 Ma- may be found intact within two distinct patches in an elongated pattern stretching for roughly 100 km underneath the divide.

Our inferred geothermal flux field is generally warmer than prior published estimates for this region (Martos et al., 2017; Shapiro & Ritzwoller, 2004; An et al., 2015; Fox-Maule et al., 2005). While the average offset with the aeromagnetic estimate (Martos et al., 2017) can be explained by the difference between the smoothed gridded topography used as model input and the deep subglacial valleys present in reality, the aeromagnetic estimate was the highest of the prior estimates, and a number of local hot spots remain even after we corrected for this bias. Fundamentally, the radar observations of copious subglacial water and basal freeze-on require a dynamic bed with many valleys at the melting point; this sort of dynamic basal environment is inconsistent with an extremely low geothermal flux from a uniformly cold craton. Spatial heterogeneity in geothermal flux is an important control on the thermal structure and basal hydrology of the ice sheet, and therefore observational datasets that sample aspects of the basal hydrological system can in turn be used to constrain spatial heterogenity in geothermal flux.

In this paper and in our companion paper (Wolovick et al., in review), we have demonstrated that it is possible to combine many disparate sources of information into a single self-consistent picture of the ice sheet and basal hydrology. The combination of observational constraints with a physically consistent forward model can yield important insights about the ice sheet state and history, allowing us to estimate the forcings that have acted on the ice sheet, along with the uncertainty and skewness of the probability distribution of those forcings, as well as giving us a detailed picture of the resulting state of the ice sheet. This nuanced picture allows us to predict the ice sheet thermal structure and flow field, the basal melt (or freezing) rate and water flux, and the distribution of old ice and deformation within the body of the ice sheet.

Acknowledgments

This work was supported by the National Natural Science Foundation of China (No. 41941006) and COLD:Finnish Academy, #322430. Undated layer picks and echo-free zone picks were produced by Sara Wolovick. We thank all of the participants in the AGAP project for their hard work in collecting and analyzing the datasets used in this paper. MJW thanks the members of the Polar Geophysics Group at the Lamont-Doherty Earth Observatory for years of stimulating discussion about Dome A and other places. Inversion results, data constraints, and best-fit model are available at DOI:10.5281/zenodo.4072255.

References

An, M., Wiens, D. A., Zhao, Y., Feng, M., Nyblade, A., Kanao, M., … Lévêque, J.-J. (2015). Temperature, lithosphere-asthenosphere boundary, and heat flux beneath the Antarctic Plate inferred from seismic velocities. *Journal of Geophysical*

Research: Solid Earth, *120*(12), 8720–8742. doi: 10.1002/2015JB011917
Bell, R., Ferraccioli, F., Creyts, T., Braaten, D., Corr, H., Das, I., … Wolovick, M. (2011). Widespread persistent thickening of the East Antarctic Ice Sheet by freezing from the base. *Science*, *331*(6024), 1592–1595. doi: 10.1126/science.1200109
Bingham, R. G., Vaughan, D. G., King, E. C., Davies, D., Cornford, S. L., Smith, A. M., … Shean, D. E. (2017). Diverse landscapes beneath Pine Island Glacier influence ice flow. *Nature Communications*, *8*(1), 1618. doi: 10.1038/s41467-017-01597-y
Bo, S., Siegert, M., Mudd, S., Sugden, D., Fujita, S., Xiangbin, C., … Yuansheng, L. (2009). The Gamburtsev mountains and the origin and early evolution of the Antarctic Ice Sheet. *Nature*, *459*(7247), 690–693. doi: 10.1038/nature08024
Comiso, J. C. (2000, May). Variability and trends in Antarctic surface temperatures from in situ and satellite infrared measurements. *Journal of Climate*, *13*(10), 1674–1696. doi: 10.1175/1520-0442
Creyts, T. T., Ferraccioli, F., Bell, R. E., Wolovick, M., Corr, H., Rose, K. C., … Finn, C. (2014). Freezing of ridges and water networks preserves the Gamburtsev Subglacial Mountains for millions of years. *Geophysical Research Letters*, *41*(22), 8114–8122. doi: 10.1002/2014GL061491
Dansgaard, W., & Johnson, S. (1969). A flow model and a timescale for the ice core from Camp Century, Greenland. *Journal of Glaciology*, *8*(53), 215–223.
Ferraccioli, F., Finn, C., Jordan, T., Bell, R., Anderson, L., & Damaske, D. (2011). East Antarctic rifting triggers uplift of the Gamburtsev Mountains. *Nature*, *479*(7373), 388–U139. doi: 10.1038/nature10566
Fischer, H., Severinghaus, J., Brook, E., Wolff, E., Albert, M., Alemany, O., … Kawamura, K. (2013, November). Where to find 1.5 million yr old ice for the IPICS "Oldest-Ice" ice core. *Climate of the Past*, *9*(6), 2489–2505. doi: 10.5194/cp-9-2489-2013
Fox-Maule, C., Purucker, M. E., Olsen, N., & Mosegaard, K. (2005). Heat flux anomalies in Antarctica revealed by satellite magnetic data. *Science*, *309*(5733), 464–467. doi: 10.1126/science.1106888
Fretwell, P., Pritchard, H. D., Vaughan, D. G., Bamber, J. L., Barrand, N. E., Bell, R., … Fujita, S. (2013). Bedmap2: improved ice bed, surface and thickness datasets for Antarctica. *The Cryosphere*, *7*(1), 375 – 393. doi: 10.5194/tc-7-375-2013
Gillet-Chaulet, F., & Hindmarsh, R. C. A. (2011). Flow at ice-divide triple junctions: 1. Three-dimensional full-Stokes modeling. *Journal of Geophysical Research: Earth Surface*, *116*(F2), n/a–n/a. doi: 10.1029/2009JF001611
Jacobson, H., & Waddington, E. (2005). Recumbent folding of divide arches in response to unsteady ice-divide migration. *Journal of Glaciology*, *51*(173), 201–209. doi: 10.3189/172756505781829412
Jacobson, H., & Waddington, E. D. (2004). Recumbent folding in ice sheets: a core-referential study. *Journal of Glaciology*, *50*(168), 3–16. doi: 10.3189/172756504781830204
Jaupart, C., & Mareschal, J.-C. (2007). 6.05 - Heat flow and thermal structure of the lithosphere. In G. Schubert (Ed.), *Treatise on Geophysics* (pp. 217 – 251). Amsterdam: Elsevier.
Jouzel, J., Masson-Delmotte, V., Cattani, O., Dreyfus, G., Falourd, S., Hoffmann, G., … Wolff, E. W. (2007). Orbital and Millennial Antarctic Climate Variability over the Past 800,000 Years. *Science*, *317*(5839), 793–796. doi: 10.1126/science.1141038
Le Brocq, A. M., Payne, A. J., & Vieli, A. (2010). An improved Antarctic dataset for high resolution numerical ice sheet models (ALBMAP v1). *Earth System Science Data*, *2*(2), 247–260. doi: 10.5194/essd-2-247-2010
Martos, Y. M., Catalán, M., Jordan, T. A., Golynsky, A., Golynsky, D., Eagles, G.,

& Vaughan, D. G. (2017). Heat Flux Distribution of Antarctica Unveiled. *Geophysical Research Letters*, *44*(22), 11,417–11,426. doi: 10.1002/2017GL075609

Meyer, C. R., & Creyts, T. T. (2017). Formation of ice eddies in subglacial mountain valleys. *Journal of Geophysical Research: Earth Surface*, *122*(9), 1574–1588. doi: 10.1002/2017JF004329

NEEM Community Members, . (2013). Eemian interglacial reconstructed from a Greenland folded ice core. *Nature*, *493*(7433), 489–494. doi: 10.1038/nature11789

Pattyn, F. (2010). Antarctic subglacial conditions inferred from a hybrid ice sheet/ice stream model. *Earth and Planetary Science Letters*, *295*(3-4), 451–461. doi: 10.1016/j.epsl.2010.04.025

Raymond, C. (1983). Deformation in the vicinity of ice divides. *Journal of glaciology*, *29*(103), 357–373.

Rignot, E., Mouginot, J., & Scheuchl, B. (2011). Ice flow of the Antarctic Ice Sheet. *Science*, *333*(6048), 1427–1430. doi: 10.1126/science.1208336

Rose, K. C., Ferraccioli, F., Jamieson, S. S. R., Bell, R. E., Corr, H., Creyts, T. T., . . . Damaske, D. (2013). Early East Antarctic Ice Sheet growth recorded in the landscape of the Gamburtsev Subglacial Mountains. *Earth and Planetary Science Letters*, *375*, 1 – 12. doi: 10.1016/j.epsl.2013.03.053

Shapiro, N. M., & Ritzwoller, M. H. (2004). Inferring surface heat flux distributions guided by a global seismic model: particular application to Antarctica. *Earth and Planetary Science Letters*, *223*(1-2), 213–224. doi: 10.1016/j.epsl.2004.04.011

Waddington, E., Bolzan, J., & Alley, R. (2001). Potential for stratigraphic folding near ice-sheet centers. *Journal of Glaciology*, *47*(159), 639–648. doi: 10.3189/172756501781831756

Wang, B., Sun, B., Martin, C., Ferraccioli, F., Steinhage, D., Cui, X., & Siegert, M. J. (2018, January). Summit of the East Antarctic Ice Sheet underlain by thick ice-crystal fabric layers linked to glacial–interglacial environmental change. In M. J. Siegert, S. S. R. Jamieson, & D. A. White (Eds.), *Exploration of Subsurface Antarctica: Uncovering Past Changes and Modern Processes* (Vol. 461, p. 0). The Geological Society of London. doi: 10.1144/SP461.1

Wolovick, M. J., Bell, R. E., Creyts, T. T., & Frearson, N. (2013). Identification and control of subglacial water networks under Dome A, Antarctica. *Journal of Geophysical Research: Earth Surface*, *118*(1), 140–154. doi: 10.1029/2012JF002555

Wolovick, M. J., & Creyts, T. T. (2016). Overturned folds in ice sheets: Insights from a kinematic model of traveling sticky patches and comparisons with observations. *Journal of Geophysical Research: Earth Surface*, *121*(5), 1065–1083. doi: 10.1002/2015JF003698

Wolovick, M. J., Creyts, T. T., Buck, W. R., & Bell, R. E. (2014). Traveling slippery patches produce thickness-scale folds in ice sheets. *Geophysical Research Letters*, *41*(24), 8895–8901. doi: 10.1002/2014GL062248

Zhao, L., Moore, J. C., Sun, B., Tang, X., & Guo, X. (2018). Where is the 1-million-year-old ice at Dome A? *The Cryosphere*, *12*(5), 1651–1663. doi: 10.5194/tc-12-1651-2018